Title: Obliquity limit of megathrust earthquakes

Authors: Xiaochuan Tian[1]*, Magali I. Billen[1],

Affiliations:

[1]Department of Earth and Planetary Sciences, University of California, Davis; Davis, CA, United States.

*Corresponding author. Email: equtian@ucdavis.edu

Abstract:

The largest earthquakes occur on subduction-zone megathrusts, where plates commonly converge obliquely to trenches and generate trench-parallel strain. How this strain is partitioned between megathrust slip and upper-plate deformation remains uncertain, hindering earthquake recurrence estimates. Here we combine global slab geometry, plate motions, and earthquake focal mechanisms to quantify convergence and megathrust slip obliquities. The results show that megathrust earthquakes slip less obliquely than plate convergence, but rarely normal to the trench, so common end-member assumptions misrepresent strain accumulation. To explain this pattern, we develop a work-minimization model of strain partitioning that predicts dip-dependent limits on megathrust slip obliquity and preferred slip directions. This framework provides a mechanical basis for estimating strain accumulation on megathrusts undergoing oblique convergence, with implications for seismic-cycle and terrane-translation models.

The paper is a non-peer reviewed preprint submitted to EarthArXiv

Main Text:

Oblique convergence is the norm

Subduction zones accommodate significant plate convergence and host the Earth's most damaging earthquakes (*1*). Many studies of seismic coupling and earthquake cycles focus on orthogonal convergence (e.g. *2–6*), yet combining a global plate motion model (*7*) with slab geometry (*8*) reveals that oblique convergence is widespread (*9*) (Fig. 1A), arising from nearby Euler poles or curved trenches (*10*). This oblique convergence generates a trench-parallel component of relative plate motion that must be accommodated either by megathrust slip or by deformation in the overriding plate. Globally, more than 50% of convergent plate boundaries have obliquities higher than 45 degrees (*11*), where trench-parallel strain is no less than its trench-normal component.

Early models proposed that above a critical convergence obliquity, trench-parallel strain is partitioned into upper-plate strike-slip faults, while below that threshold, oblique slip occurs on the megathrust itself (*10*, *12*, *13*). However, recent geodetic analyses (*9*) show that upper plates deform even at low convergence obliquity and that the relationship between obliquity and forearc deformation varies between margins. A general and quantitative framework linking convergence obliquity, subduction geometry, megathrust slip, and upper-plate deformation is lacking, hindering accurate estimations of the total strain and stress accumulation on the megathrust interface vital for seismic coupling (*2*) and recurrence (*3–6*) estimations.

Systematics of megathrust slip obliquity

We analyze systematics of global megathrust earthquake slip obliquity with three datasets: GCMT earthquake catalog (1976–2020) (*14*), Slab2 subduction interface geometry (*8*), and global plate motion models GSRM (*7*). For each interface thrust earthquake, we compute the convergence obliquity β and the earthquake slip obliquity α relative to the local down-dip azimuth of the downgoing slab (see SI: M2 for details).

Globally, most megathrust earthquakes slip less obliquely than the local plate convergence ($\alpha < \beta$; Fig.1A). This pattern persists across diverse tectonic settings, upper-plate types, slab conditions and convergence velocity. Segment-averaged slip obliquity for most subduction zones also falls below convergence obliquity (Fig.1B), indicating that a substantial fraction of trench-parallel strain is not released by the megathrust earthquakes. Meanwhile, segment-averaged megathrust earthquake slip obliquities range from 10 to 30 degrees (Fig.1B), showing that megathrust earthquakes generally do not slip in the trench-normal direction, deviating from the common simplifying assumption (*2–6*). Moreover, the difference between plate-convergence and megathrust earthquake slip directions correlates with the degree of strain partitioning (Fig. 1C), consistent with the widespread occurrence of upper-plate strike-slip earthquakes across most subduction zones (SI: Figs. S-region-A & B).

A simple analytic model for obliquity limits

These observations suggest that the trench-parallel component of the oblique strain is commonly accommodated by two coupled pathways: oblique slip on the megathrust and strike-slip deformation in the upper plate. The observed megathrust slip direction should therefore reflect the relative mechanical cost of these two deformation pathways. To quantify this tradeoff, we develop a simple analytic model (Fig. 2, see SI: M1 for details), following the spirit of Michael (1990) (*15*). The model compares the tectonic work required by two end-member deformation configurations: (a) 'Fully partitioned' deformation (Fig. 2A), in which all trench-parallel strain is released by upper-plate strike-slip faulting while the megathrust accommodates only trench-normal motion ($\alpha = 0$), and (b) 'Non-partitioned' deformation (Fig. 2B), in which all oblique strain is released by the megathrust earthquake slip ($\alpha = \beta$). Assuming earthquakes release accumulated elastic strain in a way that minimize the total tectonic work on the coupled megathrust-upper plate fault system (*16*), and following the work formulation for faulting in (*17*):

$$W_F = \bar{\tau}\mathrm{AD} \quad (1)$$

where $\bar{\tau}$ is the mean stress over rupture area A during rupture, and D is the areal averaged slip displacement. The model predicts a regime boundary $\beta_{rb}(\varphi, R)$ in obliquity–dip space when the two end-member configurations cost the same amount of energy (Fig. 2C) (see SI: M1 for details):

$$\beta_{rb}(\varphi, R) = 2\tan^{-1}[\sin\varphi/\mathrm{R}] \quad (2)$$

where $R = \bar{\tau}_T/\bar{\tau}_S$, is the effective ratio of the mean shear resistance on the megathrust to that on the upper-plate strike-slip faults, averaged in space and time. For a given R, the model predicts a dip-dependent upper bound on allowable megathrust slip obliquity: larger R indicates a relatively stronger megathrust, or weaker upper plate, so trench-parallel strain is more readily released by upper-plate deformation, and the allowable megathrust slip obliquity is reduced. Smaller R permits more oblique slip on the megathrust.

This formulation does not address how much partitioning should occur, nor does it allow finding a unique physical strength ratio for individual earthquakes. Rather, it identifies in which parameter space oblique megathrust earthquakes should not persist (the 'Partitioned' regime in Fig. 2C) because trench-parallel strain would be preferentially released in the upper plate, reducing the trench-parallel strain remaining on the megathrust. This model also predicts that shallow interfaces impose stricter limits, whereas steeper interfaces permit larger slip obliquities (Fig. 2C).

To describe the intermediate slip directions observed in natural margins (Fig. 2D), we further develop a more generalized continuous formulation that quantifies the total work as a function of slip obliquity α during a unit time dt, which can be easily integrated over earthquake cycles:

$$W_F(\alpha) = W_{FT}(\alpha) + W_{FS}(\alpha) = Vp \cdot dt \cdot [A_T\bar{\tau}_T \cdot cos\beta/cos\alpha + A_S\bar{\tau}_S \cdot (sin\beta - cos\beta \cdot tan\alpha)] \quad (3)$$

where W_{FT} and W_{FS} are tectonic work from the megathrust and upper plate strike-slip events, respectively. The rupture area of the strike-slip fault (A_S) scales with the rupture area of the thrust fault (A_T) by $A_S = A_T sin\varphi$ assuming that the depths of the brittle-ductile transition for both faults are the same and they share the same along-strike extent. Note that this assumption is useful for simplifying the derivation but may deviate from observations. We discuss its limitations and effects when interpreting data. When $\alpha = 0$, $W_F(0)$ simplifies to the partitioned end member (SI: eq.2) and when $\alpha = \beta$, $W_F(\beta)$ simplifies to the non-partitioned end member (SI: eq.3). We find an optimal slip obliquity $\alpha_o(\varphi, R)$ when the total work $W_F(\alpha)$ is minimized, by letting $\partial W_F(\alpha)/\partial\alpha = 0$:

$$\alpha_o(\varphi, R) = sin^{-1}[sin\varphi/R] \tag{4}$$

For the relevant range of $sin\varphi/R \in [0,1]$, the optimal slip obliquity satisfies $\alpha_o \leq \beta_{rb}$. Thus, the work-minimizing slip direction always lies below the obliquity limit β_{rb} (eq. 2) (Fig. 2C, S3).

Population-level estimates of effective shear resistance ratio R

Above simple analytical framework describes a first-order mechanics of strain partitioning at oblique subduction zones averaged over space and time. By contrast, individual earthquake slip may reflect local heterogeneities in stress, fault geometry and rupture history. We therefore estimate the key uncertain model parameter—the effective shear resistance ratio (R)—from population-level, long-term averaged earthquake behavior.

In the model, the obliquity limit depends on an observable dip angle (φ) and an uncertain resistance ratio (R) (eq. 2 & 4). We estimate R by fitting the observed relationship among obliquities and dip angle (α, β, φ) for a group of earthquakes. Specifically, we use the relationship between obliquity (α or β), dip and R (eq. 2) to transform the observed three-parameter space $\{\alpha, \beta, \varphi\}$ for each event into a two-parameter model space $\{R_\alpha(\alpha, \varphi), R_\beta(\beta, \varphi)\}$ (SI: M1.6, eq.8). Partitioned events satisfy $|\alpha| < |\beta|$, which is equivalent to $R_\beta < R_\alpha$. We then use a grid search to identify the best fitting value, $R^\#$, that places the largest fraction of partitioned events in the model-consistent regime ($R_\beta < R^\# < R_\alpha$), denoted as the P2 regime (SI: Fig.S4, M1.6, M2.6, M2.7).

Importantly, $R^\#$ should not be interpreted as the instantaneous stress condition for any individual earthquake. Rather, it represents a population-level estimate of an integrated first-order resistance contrast between the megathrust and upper-plate strike-slip fault systems averaged over space and time. Because subduction zone stress states are heterogeneous, R is unlikely to be constant either among margins or along a single margin. We therefore also estimate the narrowest possible R-interval that encompasses 90% of all partitioned events to reflect a possible range.

Regional tests

We apply the analytic framework to 14 global subduction zones (see results for each margin from SI: Figs. S-region-A to E), with four representative examples shown in the main text: Sumatra, Aleutians, Philippines, and Kermadec (Fig. 3). These four margins span different ranges of convergence obliquity, slab dip, inferred $R^\#$ and upper plate rock types, allowing the model to be tested beyond a single tectonic setting.

The Sumatra subduction zone exhibits trench normal convergence in the southeast, gradually transitioning to an obliquity close to 90° at its northern end. Partitioning of slip is evident from the Sumatran strike-slip fault and strike-slip earthquakes in the upper plate along significant portions of the margin (SI: Fig. S-sum-A&B) ['sum' is short for Sumatra, see Table S1 for other margins]. The Sumatra subduction zone includes 881 interface thrust earthquakes spanning a wide range of slab dip and convergence obliquity (Fig. 3A). In R_α-R_β space (Fig. S-sum-C), 761 events (86%) are classified as Partitioned ($\alpha < \beta$), while 35 events (4%) fall into the non-partitioned regime. Partitioned events account for 99.6% of the cumulative seismic moment released on the interface. Using a grid search to find $R^\#$, we find that a regime boundary β_{rb} (eq.2) with R = 1.74 ($R^\#$) explains 66% of partitioned events. As spatial-temporal variation in stress state is expected, we also find a minimal-width $R^\#$ interval that includes 90% of partitioned events. For Sumatra, this $R^\#$ interval ranges from 0.55 to 2.26 (Fig. S-sum-C). The dip-dependent regime boundary β_{rb} with R= 1.74 ($R^\#$) separates slip obliquity α from convergence obliquity β for all P2 events. The binned-averaged α as a function of dip for P2 cases aligns with the predicted dip-dependent optimal α_o with R= 1.74 ($R^\#$) (bold grey dashed lines in Fig. 3A, eq.4).

The Aleutian subduction zone is another example of a long subduction zone with substantial variation in convergence obliquity from close to normal at the eastern end to $\beta \sim 90^o$ to the west. Partitioning is evident in some regions as strike-slip events in the upper plate (Fig. S-alu-A&B). The Aleutian subduction zone includes 1052 interface thrust earthquakes. As in Sumatra, α is consistently lower than β across the margin. In the R_α-R_β regime diagram (Fig. S-alu-C), partitioned events dominate (82%). The optimal strength ratio $R^\#$=1.41 captures ~46% of partitioned events and $R^\#$ range of 0.56 to 3.56 encompasses 90% of all partitioned events, indicating greater along-strike variability than in Sumatra. Despite this variability, P2 events account for most (96%) of the cumulative seismic moment. P2-event slip obliquities for the Aleutians again follow a dip-dependent upper envelope defined by $R^\#$=1.41, with optimal α_o reproducing the trend of the binned-averaged α (Fig. 3B).

The Philippines margin, while not exhibiting the same range in obliquity as the Aleutians and Sumatra, is another example of a margin with higher subduction obliquity (β ~35–70^o), but many fewer events (N=262). Despite this smaller number of events, the optimal strength ratio of $R^\#$=1.35 captures ~98% of the partitioned events (Fig 3C & Fig. S-phi-C). In comparison for the Kermadec margin, which has a lower subduction obliquity (β ~10-30^o), the optimal kinematic ratio $R^\#$=3.75 and still captures 72% of the partitioned events. This result highlights that the concept of an obliquity limit for megathrust events applies even for low obliquity margins.

Across the 14 margins evaluated, ~68% of 10383 megathrust earthquakes, ~81.7% of M7+ events or 81.8% of M8+ events slip less obliquely than local plate convergence (Fig. S-Global). At the margin scale, binned averaged slip obliquities follow the dip-dependent optimal α_o predicted by the work-minimization formulation. Anomalous cases (red in Fig. S-region-A & C) commonly occur where convergence obliquity is low or where local structural heterogeneity is expected (e.g. seamounts indicated by short-wavelength undulations in slab depth contours). These global systematics indicate that megathrust dip exerts a first-order control on earthquake slip obliquity, supporting the work-minimization framework.

This dip dependence links the event-scale observations in Fig. 3 to the natural geometry of subduction zones illustrated in Fig. 4. In the end-member framework of Fig. 2, partitioned and non-partitioned deformation are treated as discrete configurations. In natural subduction zones, however, the megathrust is curved and commonly steepens with depth. Shallow, low-dip portions of the interface favor forearc translation and strong upper-plate partitioning, resulting in low megathrust slip obliquity. Down-dip, increasing megathrust dip allows a larger trench-parallel component of motion to remain on the megathrust, so partitioning decreases and α increases. Therefore, the analytic model provides a physical explanation for why megathrust earthquakes, which sample a range of interface dips, slip in between the directions of the fully partitioned and non-partitioned end members.

Consistency with b-value stress proxies

As an independent check on the inferred resistance ratio, we compare our population-level $R^{\#}$ values with stress proxies estimated from earthquake b-values. This comparison is motivated by global observations that b-values in subduction zones vary systematically with slab properties and the normal force acting on the megathrust (*18*), and by the empirical stress dependence of b-values (*19*). The resulting comparison shows an encouraging first-order correspondence between slip-direction-derived $R^{\#}$and b-value-derived stress ratios for several well-sampled margins (Fig. S6). However, we treat this relationship as tentative rather than as a validation of $R^{\#}$. The two quantities measure different aspects of the fault system: $R^{\#}$ reflects the population-level obliquity limit, whereas b-values reflect magnitude-frequency statistics that are sensitive to catalog completeness, event classification, stress heterogeneity, fluids, roughness, coupling, and aseismic deformation. The apparent correlation therefore points to an exciting direction for future work but requires more rigorous testing and refined b-value methods before it can be used to directly infer megathrust or upper-plate fault resistance.

Implications

Our results revise the classical threshold view of strain partitioning in oblique subduction. Earlier models suggested a critical convergence obliquity above which trench-parallel strain is accommodated by upper-plate strike-slip faulting (*10*, *12*, *13*). Our analysis shows that this transition also depends on slab dip and the effective resistance ratio between the megathrust and upper-plate faults. Because subduction interfaces are usually shallow near the trench, even low to moderate obliquity can promote upper-plate deformation when the megathrust is relatively strong. This provides a mechanical explanation for recent global observations that forearc deformation correlates with subduction obliquity and that significant upper-plate deformation need not require very high obliquity (*9*). Local complexities produce scatter, but they do not erase the first-order relationship between slab geometry and megathrust obliquity.

The work-minimization model also clarifies why megathrust slip directions are generally intermediate between the two commonly assumed end members: both end members consume more energy than the optimal megathrust slip direction (α_o eq.4). Therefore, megathrust earthquakes usually slip less obliquely than plate convergence; and assuming full plate-parallel slip overestimates the trench-parallel component of strain accumulated on the megathrust interface. Meanwhile, megathrust earthquakes also rarely slip completely normal to the trench, so assuming the pure orthogonal direction neglects part of the oblique strain that remains on the megathrust. Hence, both assumptions can bias estimates of strain accumulation, seismic coupling, and seismic cycle at oblique subduction zones.

This framework is especially useful for evaluating slip deficit and recurrence interval for margins with limited historical megathrust seismicity. Cascadia provides a simple illustrative example. According to USGS (*20*), the last great Cascadia earthquake occurred on 26 January 1700, with an estimated magnitude of $M8.7$–9.2, and U.S. Geological Survey's National Seismic Hazard Model uses an approximately 500-year recurrence interval for full-margin $M9$ ruptures. Convergence obliquity varies along the Cascadia margin, but if we take a representative convergence obliquity of 45° and assume future megathrust earthquakes slip at an optimal obliquity of 20°, then the strain accumulation rate along the actual megathrust slip direction would be $V_p\cos\ 45°/\cos\ 20° \approx 0.75V_p$, where Vp is the plate-convergence rate. In this case, an analysis based on the full convergence rate V_p would underestimate the recurrence time by about 33%; for example, 500 years should be corrected to 665 years. Alternatively, if assuming only orthogonal convergence with a rate of $V_p\cos\ 45°$, the recurrence time would be overestimated by about $1/\cos\ 20° - 1 \approx$ 6%, 500 years should be corrected to approximately 470 years. This calculation is not intended as a revised Cascadia forecast. Rather, it illustrates that the assumed megathrust slip direction can introduce tens-of-percent differences in slip-deficit budgets and recurrence-time estimates, especially in oblique margins where the true slip direction deviates significantly from the fully partitioned and non-partitioned end members.

Over geologic time, the same dip-dependent mechanism provides a mechanical basis for trench-parallel terrane translation. Modern forearc slivers bounded by a trench and arc-parallel strike-slip fault are suggested to accumulate ≥1000 km of transport during long-lived subduction (*21*). Such distances are comparable to those invoked in Cordilleran terrane-translation debates, including the Baja–British Columbia hypothesis, for which even moderate reconstructions require ~1000 km of post–mid-Cretaceous motion (*22*). Because shallow megathrust dips favor off-interface accommodation of trench-parallel strain, our model provides a mechanical pathway for large forearc translations without requiring extreme convergence obliquity (Fig. 4). It links earthquake-scale strain partitioning to long-term forearc transport for terrane translation.

More broadly, the agreement between observed megathrust slip obliquities and a work-minimization model supports the idea that simple energetic principles can organize fault-system behavior at subduction-zone scale. Work minimization has been used to explain fault-system evolution across tectonic settings (*16*, *23*); here it provides a quantitative framework for linking slab dip, effective fault resistance ratio, megathrust slip direction, and upper-plate deformation. Given the simplicity of the analytic framework and the complexity of real subduction systems, the agreement between predicted limits and observed megathrust slip obliquity is encouraging and suggests that slab dip is a previously underappreciated controlling parameter in oblique subduction tectonics and megathrust seismicity.

References and Notes

1. E. A. Wirth, V. J. Sahakian, L. M. Wallace, D. Melnick, The occurrence and hazards of great subduction zone earthquakes. *Nature Reviews Earth & Environment* **3**, 125–140 (2022).
2. C. H. Scholz, J. Campos, The seismic coupling of subduction zones revisited. *Journal of Geophysical Research: Solid Earth* **117** (2012).
3. J.-P. Avouac, From Geodetic Imaging of Seismic and Aseismic Fault Slip to Dynamic Modeling of the Seismic Cycle. *Annual Review of Earth and Planetary Sciences* **43**, 233–271 (2015).
4. K. Wang, Y. Hu, J. He, Deformation cycles of subduction earthquakes in a viscoelastic Earth. *Nature* **484**, 327–332 (2012).
5. S. Li, L. Chen, How Long Can the Postseismic and Interseismic Phases of Great Subduction Earthquake Sustain? Toward an Integrated Earthquake-Cycle Perspective. *Geophysical Research Letters* **50**, e2023GL103976 (2023).
6. R. Govers, K. P. Furlong, L. van de Wiel, M. W. Herman, T. Broerse, The Geodetic Signature of the Earthquake Cycle at Subduction Zones: Model Constraints on the Deep Processes. *Reviews of Geophysics* **56**, 6–49 (2018).
7. C. Kreemer, G. Blewitt, E. C. Klein, A geodetic plate motion and Global Strain Rate Model. *Geochemistry, Geophysics, Geosystems* **15**, 3849–3889 (2014).
8. G. P. Hayes, G. L. Moore, D. E. Portner, M. Hearne, H. Flamme, M. Furtney, G. M. Smoczyk, Slab2, a comprehensive subduction zone geometry model. *Science* **362**, 58–61 (2018).
9. K. D. Morell, K. Gilroy, T. Finley, N. Harrichhausen, Subduction Zone Obliquity Dictates Global Trench-Parallel Inner Forearc Deformation. *AGU Advances* **6**, e2024AV001468 (2025).
10. R. McCaffrey, Oblique plate convergence, slip vectors, and forearc deformation. *Journal of Geophysical Research: Solid Earth* **97**, 8905–8915 (1992).
11. M. Philippon, G. Corti, Obliquity along plate boundaries. *Tectonophysics* **693**, 171–182 (2016).
12. T. J. Fitch, Plate convergence, transcurrent faults, and internal deformation adjacent to Southeast Asia and the western Pacific. *J. Geophys. Res.* **77**, 4432–4460 (1972).
13. J. P. Platt, Mechanics of oblique convergence. *J. Geophys. Res.* **98**, 16239–16256 (1993).
14. G. Ekström, M. Nettles, A. M. Dziewoński, The global CMT project 2004–2010: Centroid-moment tensors for 13,017 earthquakes. *Physics of the Earth and Planetary Interiors* **200–201**, 1–9 (2012).

15. A. J. Michael, Energy constraints on kinematic models of oblique faulting: Loma Prieta versus Parkfield-Coalinga. *Geophysical Research Letters* **17**, 1453–1456 (1990).

16. M. L. Cooke, E. H. Madden, Is the Earth Lazy? A review of work minimization in fault evolution. *Journal of Structural Geology* **66**, 334–346 (2014).

17. C. H. Scholz, *The Mechanics of Earthquakes and Faulting* (Cambridge university press, 2019; https://books.google.com/books?hl=en&lr=&id=ynWIDwAAQBAJ&oi=fnd&pg=PR11&dq=info:dAQPv-g7n2AJ:scholar.google.com&ots=ExSwXKRxaz&sig=nMzBxGHicknA2tjc2_8CufqFeSE).

18. T. Nishikawa, S. Ide, Earthquake size distribution in subduction zones linked to slab buoyancy. *Nature Geosci* **7**, 904–908 (2014).

19. C. H. Scholz, On the stress dependence of the earthquake *b* value. *Geophysical Research Letters* **42**, 1399–1402 (2015).

20. E. A. Wirth, A. D. Frankel, B. L. Sherrod, A. R. Grant, A. Dunham, I. P. Stone, J. Grossman, "Earthquake probabilities and hazards in the U.S. Pacific Northwest" (2025–3050, U.S. Geological Survey, 2025); https://doi.org/10.3133/fs20253050.

21. R. D. Jarrard, Terrane motion by strike-slip faulting of forearc slivers. *Geology* **14**, 780–783 (1986).

22. R. F. Butler, G. E. Gehrels, K. P. Kodama, A moderate translation alternative to the Baja British Columbia hypothesis. *GSA Today* **11**, 4 (2001).

23. M. L. Cooke, J. G. Crider, K. D. Morell, L. Karlstrom, B. J. Yanites, What Is the Energy Budget of Subduction Zone Hazards? *Reviews of Geophysics* **63**, e2024RG000848 (2025).

24. P. Wessel, J. F. Luis, L. Uieda, R. Scharroo, F. Wobbe, W. H. Smith, D. Tian, The generic mapping tools version 6. *Geochemistry, Geophysics, Geosystems* **20**, 5556–5564 (2019).

25. E. Venzke, Global Volcanism Program. [Database] Volcanoes of the World (v. 5.3.6; 26 May 2026). Distributed by Smithsonian Institution., (2025); https://doi.org/https://doi.org/10.5479/si.GVP.VOTW5-2025.5.3.

26. D. Bassett, A. B. Watts, Gravity anomalies, crustal structure, and seismicity at subduction zones: 1. Seafloor roughness and subducting relief. *Geochem Geophys Geosyst* **16**, 1508–1540 (2015).

27. L. Sawade, G. Ekström, L. Ding, M. Nettles, J. Tromp, Parsimonious Green function data bases for global centroid moment tensor inversions. *Geophys J Int* **240**, 1986–1999 (2025).

28. J. A. Álvarez-Gómez, FMC—Earthquake focal mechanisms data management, cluster and classification. *SoftwareX* **9**, 299–307 (2019).

29. L. M. Wallace, Å. Fagereng, S. Ellis, Upper plate tectonic stress state may influence interseismic coupling on subduction megathrusts. *Geology* **40**, 895–898 (2012).

30. K. Aki, P. G. Richards, *Quantitative Seismology* (2002; https://ui.adsabs.harvard.edu/abs/2002quse.book.....A/).

31. P. Virtanen, R. Gommers, T. E. Oliphant, M. Haberland, T. Reddy, D. Cournapeau, E. Burovski, P. Peterson, W. Weckesser, J. Bright, S. J. van der Walt, M. Brett, J. Wilson, K. J. Millman, N. Mayorov, A. R. J. Nelson, E. Jones, R. Kern, E. Larson, C. J. Carey, İ. Polat, Y. Feng, E. W. Moore, J. VanderPlas, D. Laxalde, J. Perktold, R. Cimrman, I. Henriksen, E. A. Quintero, C. R. Harris, A. M. Archibald, A. H. Ribeiro, F. Pedregosa, P. van Mulbregt, SciPy 1.0: fundamental algorithms for scientific computing in Python. *Nat Methods* **17**, 261–272 (2020).

32. S. Maneewongvatana, D. M. Mount, Analysis of approximate nearest neighbor searching with clustered point sets. arXiv arXiv:cs/9901013 [Preprint] (1999). https://doi.org/10.48550/arXiv.cs/9901013.

33. T. Utsu, A statistical significance test of the difference in b-value between two earthquake groups. *Journal of Physics of the Earth* **14**, 37–40 (1966).

34. K. Aki, Maximum likelihood estimate of b in the formula log N= a- bM and its confidence limits. *Bull. Earthquake Res. Inst. Univ. Tokyo* **43**, 237–239 (1965).

35. S. Tinti, P. Gasperini, The estimation of b-value of the frequency–magnitude distribution and of its 1σ intervals from binned magnitude data. *Geophys J Int* **238**, 433–458 (2024).

36. J. Woessner, S. Wiemer, Assessing the quality of earthquake catalogues: Estimating the magnitude of completeness and its uncertainty. *Bulletin of the Seismological Society of America* **95**, 684–698 (2005).

37. P. Clift, P. Vannucchi, Controls on tectonic accretion versus erosion in subduction zones: Implications for the origin and recycling of the continental crust. *Reviews of Geophysics* **42** (2004).

38. P. D. Clift, A revised budget for Cenozoic sedimentary carbon subduction. *Reviews of Geophysics* **55**, 97–125 (2017).

Acknowledgments: This work benefited greatly from discussions with Mark Behn, W. Roger Buck, Yen Joe Tan, Sarah Roeske, Eunseo Choi and Alexandre Janin. We appreciate reviewers' constructive comments.

Funding: X.T. was supported by the Lori Summa and David Awwiller Postdoctoral Research Fellowship at University of California, Davis.

Author contributions:

Conceptualization: XT, MIB

Methodology: XT, MIB

Investigation: XT, MIB

Visualization: XT

Funding acquisition: MIB, XT

Supervision: MIB

Writing – original draft: XT

Writing – review & editing: XT, MIB

Competing interests: Authors declare that they have no competing interests.

Data and materials availability: All data are presented in the main text and supplementary materials. Final source code and data will be archived as a static Zenodo repository upon publication.

Supplementary Materials

Materials and Methods

Figs. S1 to S6

Tables S1

Supplementary Text

Fig. S-region-A to E (70 figures)

Fig. S-Global

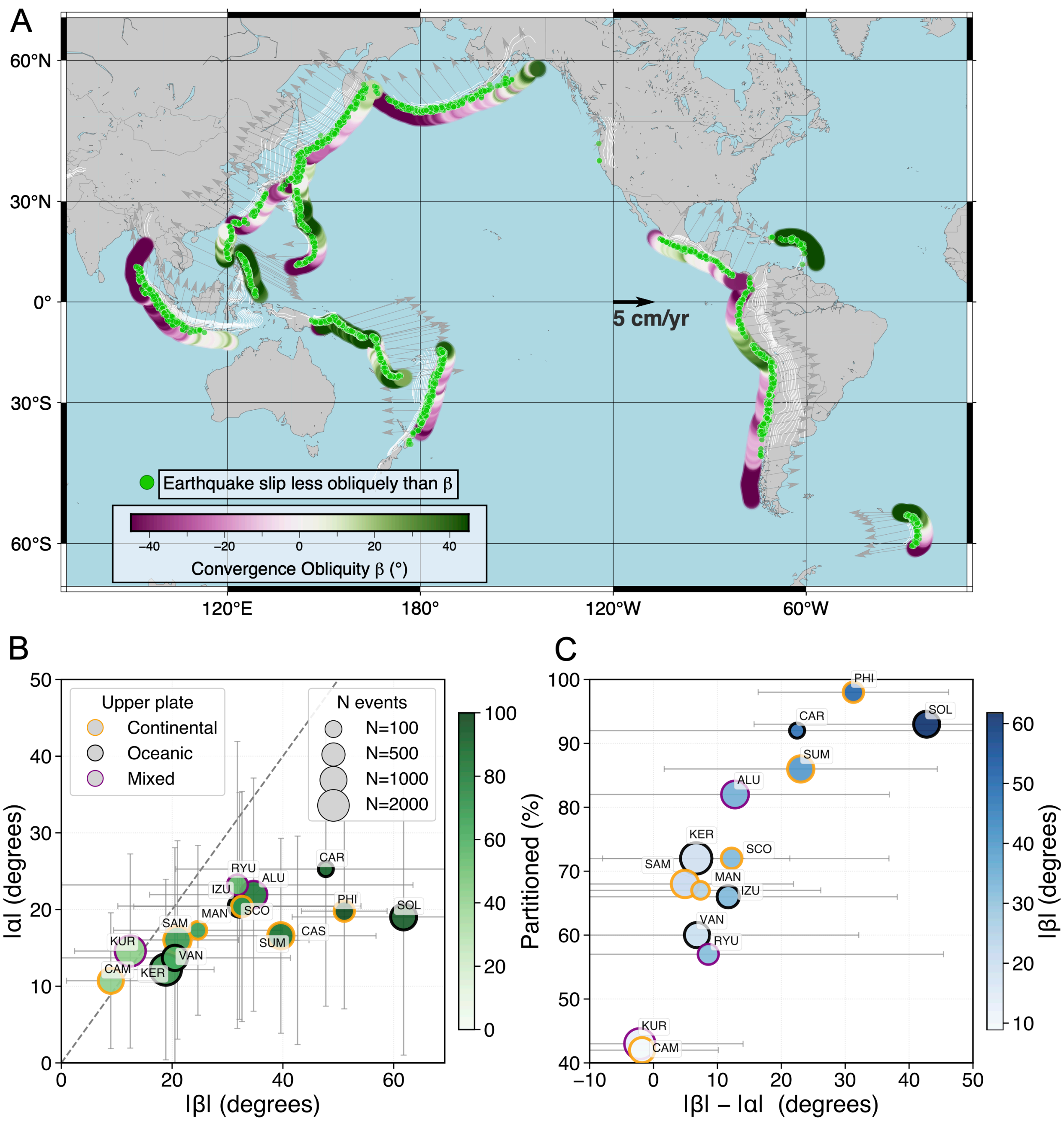

Figure. 1 Global subduction zone convergence obliquity versus megathrust earthquake slip obliquity. The green dots in the global map (**A**) show megathrust earthquakes that slip less obliquely than the local convergence. Plate velocities are calculated by 'GAGE Plate Motion Calculator' using GSRM v2.1(*7*). Megathrust interface depth contours are from Slab2 (*8*). Map plotted with GMT (*24*). See SI for detailed maps of each subduction zones. (**B**) Segment-averaged megathrust earthquake slip obliquity |α| versus convergence obliquity |β|, colored by the percentage of total number of partitioned events (α<β) over all thrust events on the megathrust. The dashed line indicates α=β. (**C**) Percentage of partitioned events versus difference between |β| and |α|, colored by |β|. For B & C, circle sizes reflect total number of events considered. Circle outline colors show major upper-plate arc volcanic rock types inferred from Smithsonian Global Volcanism Program volcano rock-type records (*25*).

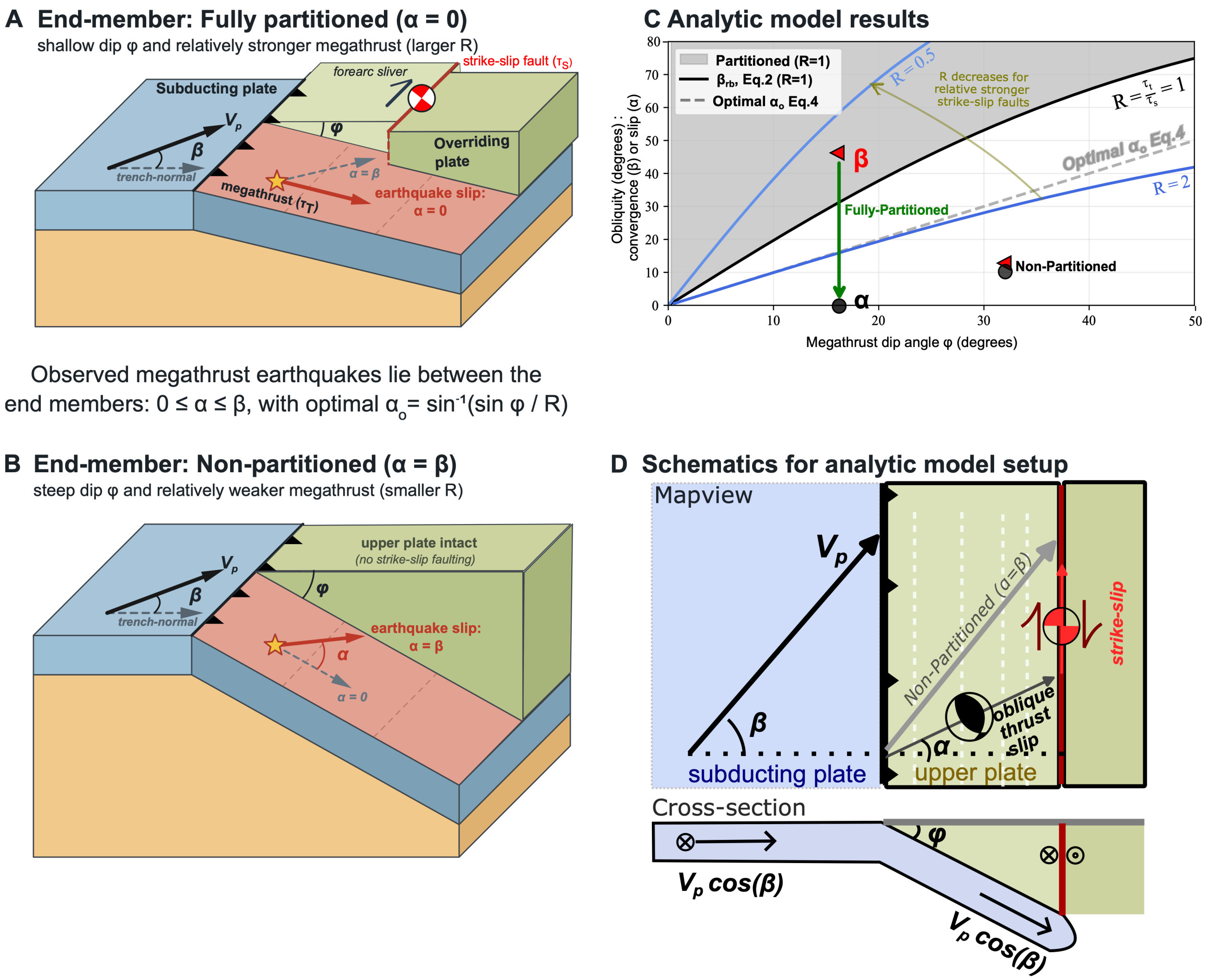

Fig 2. Analytic model for obliquity limits of megathrust earthquake slip. (A) Fully partitioned end member, in which the trench-parallel component of oblique convergence is fully accommodated by upper-plate strike-slip faulting with average resistance $\bar{\tau}_S$, resulting in trench-normal ($\alpha = 0$) earthquake slip on the megathrust interface with average resistance $\bar{\tau}_T$. This configuration is favored for shallow megathrust dip φ and/or relatively stronger megathrust resistance, corresponding to larger $R = \bar{\tau}_T / \bar{\tau}_S$. **(B)** Non-partitioned end member, in which the upper plate remains intact, and the megathrust accommodates all trench-parallel component of the oblique convergence ($\alpha = \beta$). This configuration is favored for steeper megathrust dip and/or relatively weaker megathrust, corresponding to smaller R. (**C**) Given φ and R, the analytic model predicts a 'Partitioned' regime shown as the grey shaded region above the regime boundary β_{rb} (Eq.2 assuming R=1). This 'Partitioned' regime is a forbidden zone for megathrust earthquake slip obliquities (α) because when convergence obliquities β are above the obliquity limit β_{rb}, the trench-parallel strain is predicted to be preferentially released by strike-slip faulting in the upper plate until the remaining trench-parallel strain results in a megathrust earthquake slip obliquity α below the regime boundary β_{rb}. Note that larger R values indicate relatively stronger megathrust and lowering the maximum possible megathrust earthquake slip obliquity α. Two end member scenarios are illustrated with the schematic pairs: red triangles for convergence obliquities β and the associated black circles for the slip obliquities α at the same dip angles of 16 or 32 degrees. **(D)** Schematic analytic model setup in mapview and cross-section view. The megathrust earthquake slip obliquity is α, convergence obliquity is β and the dip angle of the subduction is φ. Partitioning transfers part of the trench-parallel component to upper-plate strike-slip faulting.

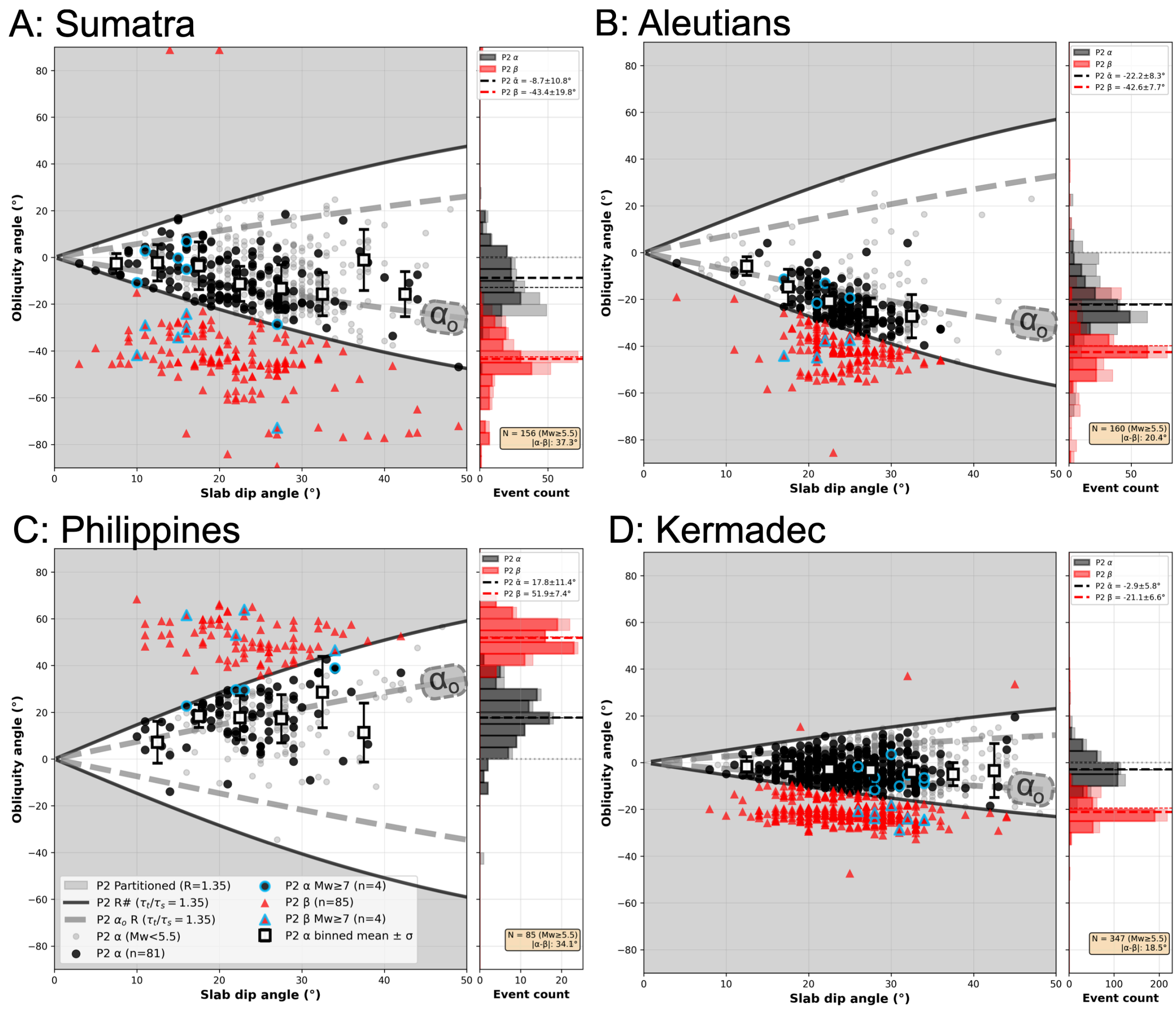

Fig. 3 | Dip-dependent upper bounds for megathrust slip obliquity. (A: Sumatra; **B**: Aleutians; **C**: Philippines; **D:** Kermadec**)** Pairs of earthquake slip obliquity α (black circles) and convergence obliquity β (red triangles) versus slab dip φ. P2 events (Fig. S4) are partitioned earthquakes for which $R_\beta < R^\# < R_\alpha$, meaning that the observed convergence and slip obliquities bracket the analytic obliquity limit β_{rb} (Eq.2 with R=$R^\#$), consistent with the theory prediction. Bold grey dashed lines are the optimal slip obliquity α_o (Eq.4 with R=$R^\#$). The observed binned-average slip obliquity α are also plotted as white rectangles. Histograms highlight separation of obliquities for megathrust events (Mw≥5.5): earthquake slip obliquity α (black) versus convergence obliquity β (red), with dashed lines indicating the averages.

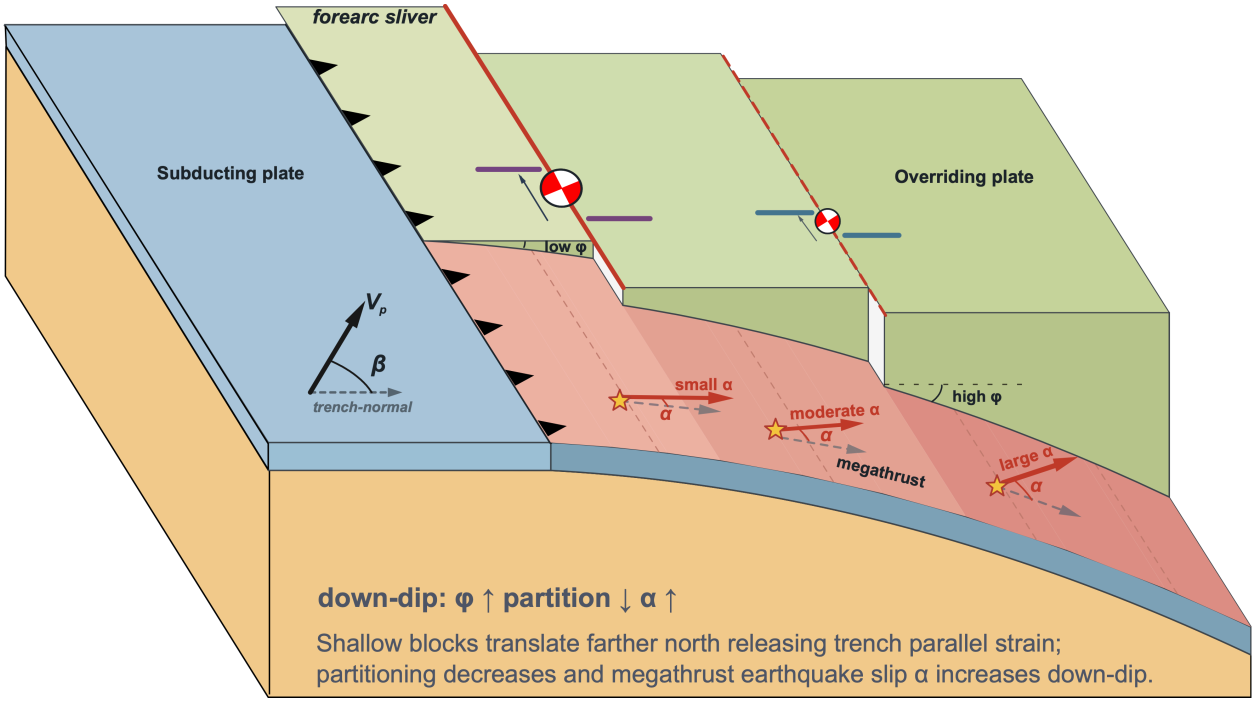

Fig. 4 Schematic strain partitioning between megathrusts and upper plate strike-slip faults at obliquely converging subduction zones. Natural subduction zones commonly have curved megathrusts whose dip φ increases with depth. In this geometry, shallow forearc blocks tend to be translated in the trench-parallel direction due to upper plate strike-slip faulting. This strike-slip deformation releases much of the trench-parallel component of the oblique plate convergence. The resulting megathrust earthquake slip obliquity α is low. Down-dip, increasing interface dip permits larger megathrust slip obliquity (larger α).

Supplementary Materials for

Obliquity limit of megathrust earthquakes

Authors: Xiaochuan Tian[1]*, Magali I. Billen[1]

Corresponding author: equtian@ucdavis.edu

The PDF file includes:

Materials and Methods
Figs. S1 to S6
Tables S1

Other Supplementary Materials for this manuscript include the following:

Supplementary Text
Fig. S-region-A to E (70 figures)
Fig. S-Global

Materials and Methods

M1 Theoretical framework

M1.1 Problem formulation

We consider an oblique subduction system in which a plate converges toward a trench with velocity V_p at an angle β relative to the trench-normal direction (Figure S1). Earthquake slip on the megathrust occurs at an angle α relative to the trench-normal, and the subduction interface dips at an angle φ. Oblique convergence can be accommodated either by (i) oblique slip on the megathrust (non-partitioned case) (α = β), or (ii) full partitioning between trench-normal thrusting and trench-parallel strike-slip faulting in the upper plate, similar to Michael, (1990) (*15*) (α = 0). Our goal is to quantify how deformation partitions between these two end-member modes (Fig. 2A&B).

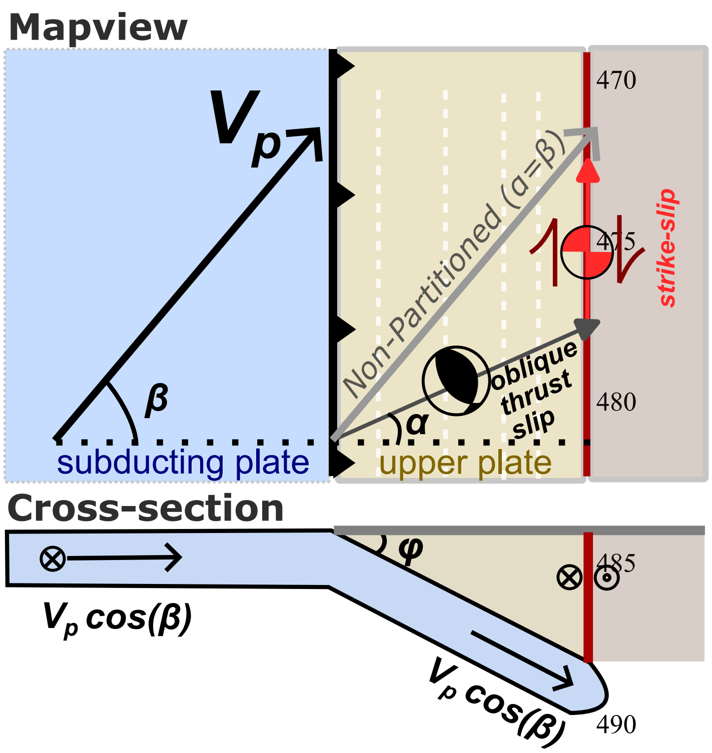

***Figure S1**. Mapview and cross-section view of a simplified oblique subduction zone. The oblique motion can be partitioned into pure normal and upper plate strike-slip motions or solely accommodated on the subduction interface by oblique thrusting. The convergence obliquity is β and the dip angle of the subduction is φ.*

M1.2 Energy formulation for two end-member modes

We assume that the configurations of tectonic deformation minimize total mechanical work (*16*), approximated as $W = \bar{\tau}AD$ (*17*), where $\bar{\tau}$ is mean stress averaged temporally during rupture duration dt and spatially over rupture area A, and D is displacement. We compare two end-member configurations over a representative time interval dt.

1. Fully partitioned (subscript 'p') case (Fig. 2A):

The displacement on the thrust fault is $D_t = V_p \cdot cos\beta \cdot dt$, and the strike-slip fault displacement is $D_s = V_p \cdot sin\beta \cdot dt$ (subscript 't' and 's' stand for thrust and strike-slip faults). The total work for partitioned case:

$$W_p = \tau_t \cdot A_t \cdot D_t + \tau_s \cdot A_s \cdot D_s \quad (1)$$

Assuming geometric scaling between thrust and strike-slip fault areas is $A_s = A_t \cdot \sin\varphi$ (at shallow depths when depths of brittle-ductile transition for both faults are the same and share the same along-strike extent), work for fully partitioned case reduces to:

$$W_p = A_t \cdot V_p \cdot dt \, [\, \tau_t \cdot cos\beta + \tau_s \cdot sin\varphi \cdot sin\beta \,] \tag{2}$$

<u>2. Non-partitioned (subscript 'np') case (Fig. 2B):</u>

The total work when all deformation is accommodated on the thrust fault by oblique megathrust slip (upper plate has no deformation) with total displacement of $V_p \cdot dt$:

$$W_{np} = \tau_t \cdot A_t \cdot V_p \cdot dt \tag{3}$$

M1.3 Obliquity limit from energetic competition

Partitioning becomes energetically favorable when $W_p < W_{np}$ (*16*). Defining the strength ratio $R = \tau_t/\tau_s$, this inequality yields an upper bound on allowable megathrust slip obliquity where the energy costs for the two end-member cases become the same:

$$\beta_{max}(\varphi, R) = 2\tan^{-1}[\sin\varphi/R] \tag{4}$$

This relation defines a forbidden region $\beta(\varphi, R) > 2\tan^{-1}[\sin\varphi/R]$ (Grey shaded zone 'Partitioned') in obliquity–dip space ($\beta[\varphi]$) where megathrust slip cannot accommodate all deformation (Figure S2, Fig. 2C), and partial trench-parallel strain must be partitioned into upper-plate strike-slip faulting. The isochrons of different R values show that the area of this forbidden region (Partitioned regime) becomes larger when a megathrust becomes stronger relative to its adjacent upper plate strike-slip fault (larger R), limiting the maximum megathrust slip obliquity (α) to lower values.

Note that a simpler condition for the Partitioned regime:

$$R_F > 1/tan[\beta/2] \tag{5}$$

relating force ratio ($R_F = F_t/F_s$) and convergence obliquity can be found by considering the same inequality $W_p < W_{np}$, where $F_t = \tau_t \cdot A_t$ and $F_s = \tau_s \cdot A_s$ similar to ref. (10). In this case, one does not need to explicitly include the dependence on dip ($A_s = A_t \cdot \sin\varphi$). However, because force is not as directly measurable as does the dip angle, we prefer to explicitly include the dip angle as a model controlling parameter to better compare with data.

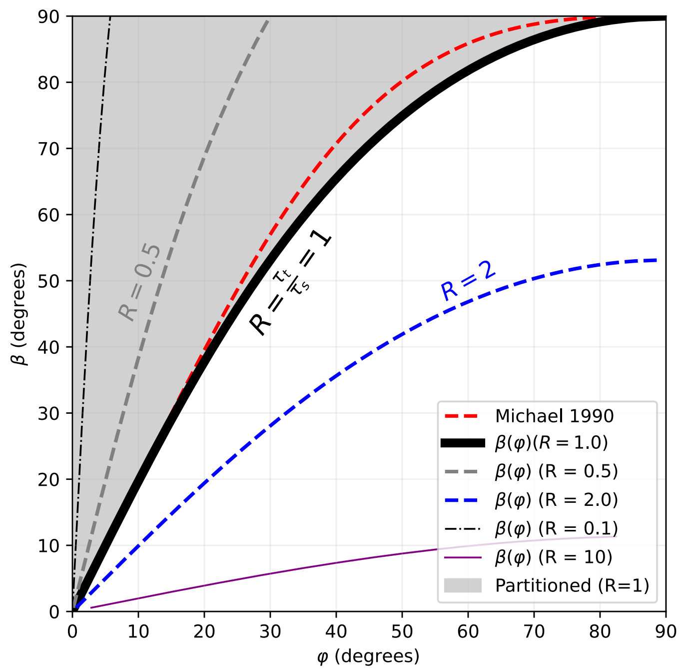

Figure S2*. Given β, φ,* *and R (ratio between the average shear stresses on the megathrust (τ_t) versus the strike-slip fault (τ_s) in the upper plate), the analytic model predicts a grey shadowed region above the bold black curve (here assuming R=1) as the regime of 'Partitioned', in which the combination of obliquity and dip is favorable for the partitioned end-member regime. Hence under the model assumptions, this is a forbidden zone for megathrust earthquakes to exist because the trench-parallel component should be released by strike slip faulting in the upper plate until α is below the (R=1) curve. Note larger R values, indicate a relatively stronger megathrust, and lowering the possible megathrust earthquake slip obliquity.*

M1.4 Continuous formulation of partial partitioning

Natural systems exhibit a continuum between the two end members ($0 \leq \alpha \leq \beta$). We therefore formulate total work as a function of slip obliquity α:

$$W(\alpha) = V_p \cdot dt \left[\tau_t \cdot A_t \cdot cos\beta \,/\, cos\alpha + \tau_s \cdot A_s \cdot (sin\beta - cos\beta \cdot tan\alpha) \right] \quad (6)$$

This expression accounts for work done by both the oblique slip on the megathrust and the residual trench-parallel motion accommodated by upper-plate strike-slip faulting (Figure S1). When $\alpha = 0$, $W(0)$ simplifies to partitioned end member W_p (eq. 2) and when $\alpha = \beta$, $W(\beta)$ simplifies to non-partitioned end member W_{np} (eq. 3).

M1.5 Optimal slip obliquity

The energetically optimal slip direction (α_o) is obtained by minimizing W(α) with respect to α, $\partial W_F(\alpha)/\partial\alpha = 0 \;\Rightarrow$

$$\alpha_o(\varphi, R) = sin^{-1}[sin\varphi / R] \quad (7)$$

This solution predicts that the optimal (energetically minimized) slip obliquity increases with slab dip and decreases with increasing relative megathrust strength, and it always satisfies that $\alpha_o < \beta_{max}$ for meaningful range of $sin\varphi/R$ from 0 to 1 (Figure S3).

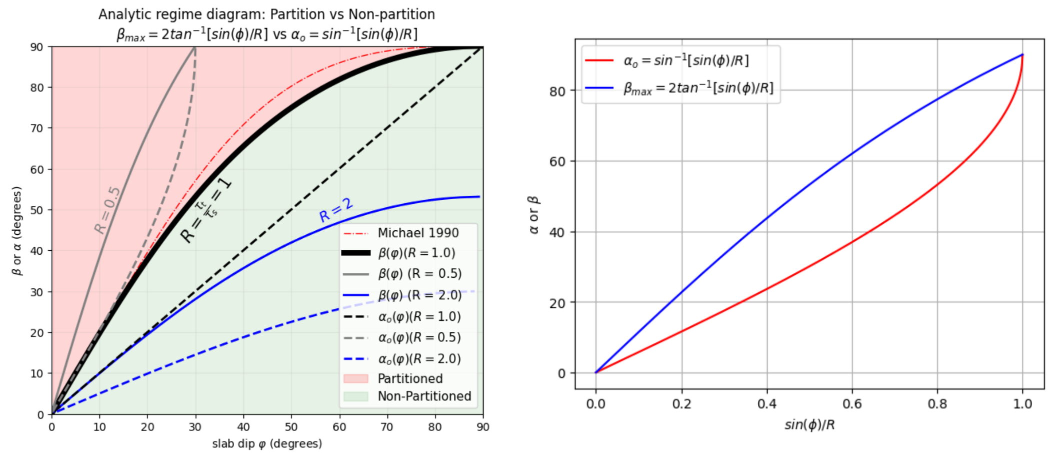

***Figure S3**. Comparing regime boundary $\beta_{max}(\varphi, R)$(eq. 4) and $\alpha_o(\varphi, R)$ over meaningful range of $sin\varphi/R$.*

M1.6 Regime classification

To facilitate classification of megathrust earthquakes under the theoretical framework described above, we define normalized quantities that map each earthquake onto a regime diagram (Fig. S4). For each event, given measured slip obliquity α, convergence obliquity β, and slab dip φ, we define:

$$R_\alpha = sin\ \varphi/tan\ (|\alpha|/2)\ , \quad and \quad R_\beta = sin\ \varphi/tan\ (|\beta|/2) \qquad (8)$$

These expressions are obtained by rearranging the analytic obliquity limit (Eq. 4), allowing using a single value R_α or R_β to describe an earthquake's relative position in the obliquity-dip space (α, β-- φ; Fig. S2). This transformation allows all events, regardless of dip or obliquity, to be represented in a unified R_α–R_β space.

In this normalized R_α–R_β space, earthquakes are classified into three primary regimes based on their relative position to the 1:1 line ($R_\alpha = R_\beta$):

Partitioned regime ($|\alpha| < |\beta|$; $R_\alpha > R_\beta$)

Megathrust slip is less oblique than plate convergence, indicating that a portion of trench-parallel strain is accommodated outside of the megathrust, primarily by upper-plate deformation (Fig S4: green).

Non-partitioned regime ($|\alpha| \approx |\beta|$; $R_\alpha \approx R_\beta$)

Oblique convergence is accommodated largely by slip on the megathrust itself (Fig S4: yellow)

Anomalous regime ($|\alpha| > |\beta|$; $R_\alpha < R_\beta$)

Earthquake slip is more oblique than convergence. These cases are not predicted by the simple model and likely reflect local heterogeneities (e.g., seamount subduction) (Fig S4: pink).

This classification directly corresponds to the colored regions shown in Fig. S4.

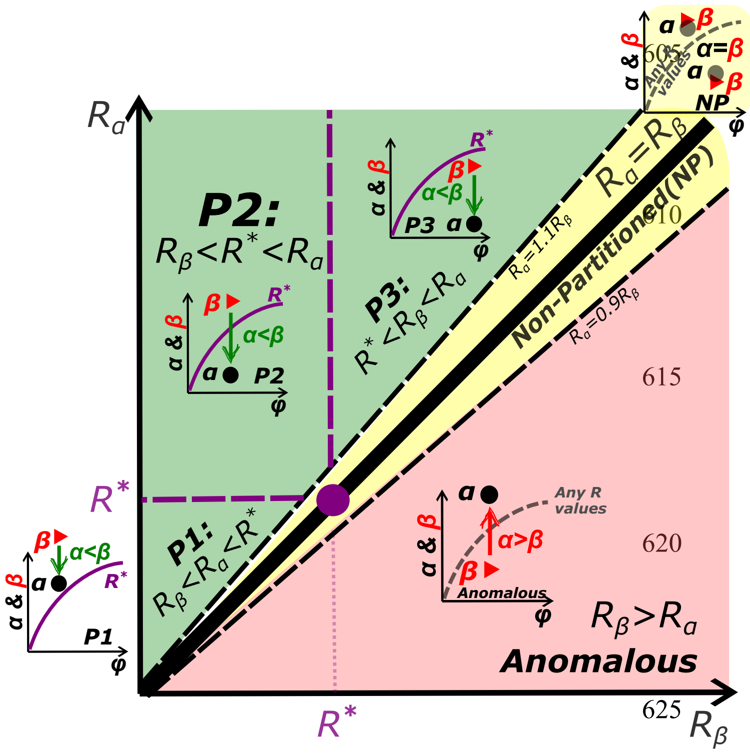

Figure S4. Regime diagram. For each megathrust earthquake, given its measured α, β' and φ, we can use the close form solution to calculate $R_\alpha = sin\ \varphi/tan\ (|\alpha|/2)$ and $R_\beta = sin\ \varphi/tan\ (|\beta|/2)$. For each event, we can locate it in the R_α-R_β regime diagram, where three major regimes arise: 1) Anomalous (red shaded) when $R_\beta > R_\alpha$, indicating |β| < |α|, which might be due to local heterogeneity (e.g. subducted seamounts); 2) Non-Partitioned (NP, yellow shaded) where $R_\alpha \approx R_\beta$ (|α| ≈|β|). 3) Partitioned (green shaded) where $R_\beta < R_\alpha$ and |β| > |α|.

Within the partitioned regime, we further define three sub-regimes relative to an effective strength ratio R^*, which characterizes the best-fit regime boundary value of R for the earthquake population that is fully consistent with the analytic model ($R_\alpha < R^* < R_\beta$). We use a grid search to find R^* such that it provides the maximum percentage count of events ($R^\#$) to fall within the P2 sub-regime:

<u>P2 (model-consistent regime): $R_\beta < R^* < R_\alpha$</u>

Events in this regime are consistent with the analytic model prediction for a given R^*, where the convergence obliquity is larger than the slip obliquity and the two obliquities are separated by the isochron defined by R^* and equation 4 with $R=R^*$.

<u>P1 (both obliquities above predicted curve): $R_\beta < R_\alpha < R^*$</u>

Both α and β lie above the predicted curve for R^* in Figure S2, indicating more oblique slip than predicted by the best fit value R^*. These cases may reflect spatial heterogeneities, e.g., locally stronger upper-plate fault (lower R value in equation 4, Figure S2) or temporal variation in stress conditions.

<u>P3 (below predicted curve): $R^* < R_\beta < R_\alpha$</u>

Both α and β lie below the predicted curve for R^*. These cases may reflect locally stronger megathrust coupling (higher R value in equation 4, Figure S2).

Note that the existence of P2 and P3 cases is expected as we anticipate that the relative strength ratio R to vary in space and time given the complex and heterogeneous nature of subduction zones. In addition, although R_α and R_β are expressed in terms of the strength ratio R, they should not be interpreted as physical stress ratios for individual earthquakes. Instead, R_α and R_β only represent projections of the observed obliquities onto the theoretical parameter space, which allows for quantifying R^*; and R^* represents a population-level parameter that best explains the distribution of events. This distinction is important because individual earthquakes reflect spatially and temporally variable stress states, whereas the analytic model describes first-order system-averaged behavior.

This mapping between the observed values (α, β, φ) and (R_α, R_β) for regime classification provides a quantitative way to categorize megathrust earthquakes into three major types under the context of the analytic model of strain partitioning. Mathematically, this transformation also collapses the three-parameter system (α, β, φ) into a two-parameter space (R_α, R_β), enabling direct comparison across subduction zones with different geometries using a single value R^*.

M1.7 Assumptions and limitations of the analytic model framework

The simple analytic model assumes (i) accumulated elastic strain is mainly released by slip on the two major fault systems (i.e. megathrust and upper plate strike-slip) manifested as earthquakes over a finite time interval (e.g. an earthquake cycle), (ii) spatial-temporal averaged shear stresses on the fault interfaces characterize relative strength of the two major faults, (iii) effective ratio for fault areas scales geometrically with slab dip, and (iv) dynamic rupture complexity and heterogeneity are not explicitly modeled. The framework is therefore intended to capture an integrated first-order, system-averaged characteristics rather than to predict individual events.

M2. Data and Processing

M2.1 Data sources

We compiled a catalog of global subduction-interface thrust earthquakes for analyzing the systematics of strain partitioning by combining earthquake focal mechanisms, slab geometry, and plate convergence directions. Earthquake source parameters were taken from the Global Centroid Moment Tensor (GCMT) catalog from year 1976 to 2020, which includes a total of 56,830 events and a minimum magnitude of *Mw* 4.3 (*14*). For each event, we used earthquake information like centroid and hypocenter location and depth, magnitude, and moment tensor. Subduction-interface geometry was obtained from Slab2 (*8*), including slab depth, dip, strike, thickness, and depth uncertainty. Plate convergence directions were calculated using GSRMv2.1 (*7*) from the UNAVCO 'GAGE plate motion calculator' and sampled slightly seaward and along the subduction trenches (*26*). For each subduction zone, events were first selected using the geographic bounds of a slab from Slab2 and restricted to shallow (<70 km) seismogenic depths (*27*).

M2.2 Categorize earthquakes relative to slab geometry

We first use vertical distance away from slab interface to identify events that likely happened on the megathrust interface. For each GCMT event, slab properties (e.g. depth) are queried from Slab2 model at the geographically nearest grid from the event longitude and latitude. We used both centroid- and hypocenter-based comparisons to evaluate whether an event was located on the slab interface. The vertical distance between earthquake depth and the slab depth was compared with the local Slab2 depth uncertainty. Events were retained as on-slab candidates if either the centroid depth or hypocenter depth was within one Slab2 depth uncertainty of the modeled slab surface:

$$|\Delta z_{\text{centroid}}| < \sigma_{\text{Slab2}} \quad \text{or} \quad |\Delta z_{\text{hypocenter}}| < \sigma_{\text{Slab2}} \tag{9}$$

where Δz is the depth difference between the earthquake and Slab2 interface and σ_{Slab2} is the local Slab2 depth uncertainty. We use this relaxed union criterion to avoid excluding interface events whose centroid or hypocenter alone may be offset slightly from the modeled interface. For $|\Delta z| > \sigma_{\mathrm{Slab2}}$, we further categorize them as above or below slab interface. Finally, we use focal mechanism to exclude events characterized as being on the interface but having a focal mechanism far from that of a megathrust earthquake (See next subsection).

M2.3 Focal-mechanism filtering and slip vector calculation

We select thrust-type earthquakes from megathrust interface events using focal mechanism geometry. The nodal-plane ambiguity was resolved by comparing the dips of two nodal planes with local Slab2 dip. The selected plane was then used to compute the slip vector.

Final interface-thrust events are obtained by applying below filtering criteria:

1. T-axis plunge $> 45°$ and P-axis plunge $<45°$ for thrust mechanism (*28*)
2. Rake ranges between $30°$ and $150°$ for removing strike-slip dominated events
3. Fault-plane dip $\leq 50°$ for removing antithetic thrust faulting in the upper plate (*29*)
4. Absolute slip obliquity $|\alpha| < 90°$ for reasonable range of slip obliquity relative to downdip direction

These filters remove normal-faulting, strike-slip-dominated, steeply dipping upper plate thrust events close to the interface while retaining events with thrust mechanisms consistent with slip on the subduction interface.

Slip vectors are calculated from strike, dip, and rake using the Aki and Richards convention (equation 4.88 in ref. (*30*)) in north-east-down coordinates. The horizontal slip azimuth for the upper plate is then rotated by 180° to represent the slip direction of the downgoing plate on the megathrust.

M2.4 Calculation of convergence and slip obliquity

For each selected earthquake, we calculated two signed obliquity angles relative to the local trench-normal / downdip direction of the slab (positive values for slip or convergence azimuths rotating clockwise from the downdip direction):

- α: earthquake slip obliquity, defined as the signed angular difference between the earthquake slip azimuth and the local Slab2 downdip azimuth.
- β: convergence obliquity, defined as the signed angular difference between the plate convergence azimuth and the local Slab2 downdip azimuth.

Angular differences are computed using a minimum-angle convention:

$$\Delta\theta = (\theta_2 - \theta_1 + 180°)\%360° - 180° \quad (10)$$

where θ_1 is the downdip direction as the reference azimuth ($0° - 360°$) and θ_2 is either the earthquake slip azimuth or the plate convergence azimuth ($0° - 360°$). Equation 10 handles azimuths near the 0°/360° boundary and return an angle difference between $-180°$ and $180°$.

Plate convergence azimuths that are associated with the megathrust earthquakes are chosen by finding the closest trench plate velocity data point using SciPY library (*31*) scipy.spatial:cKDTree algorithm (*32*).

M2.5 Dip correction for convergence obliquity

Because plate convergence β is measured seaward before entering the trench in map view whereas megathrust slip occurs on a dipping interface with dip φ, we projected the plate velocity at depth onto the map view by applying a geometric correction to get the local convergence obliquity β':

$$\beta' = \tan^{-1}(\tan\beta / \cos\varphi) \quad (11)$$

This correction accounts for the projection of trench-normal convergence after plate bending beyond the trench at the megathrust interface back onto the surface. The difference is generally small but becomes larger for steeper slabs and convergence obliquity closer to 40° (Fig. S5). In subsequent calculations of R_β, we use local convergence obliquity β' rather than the uncorrected convergence obliquity β seaward of the trench.

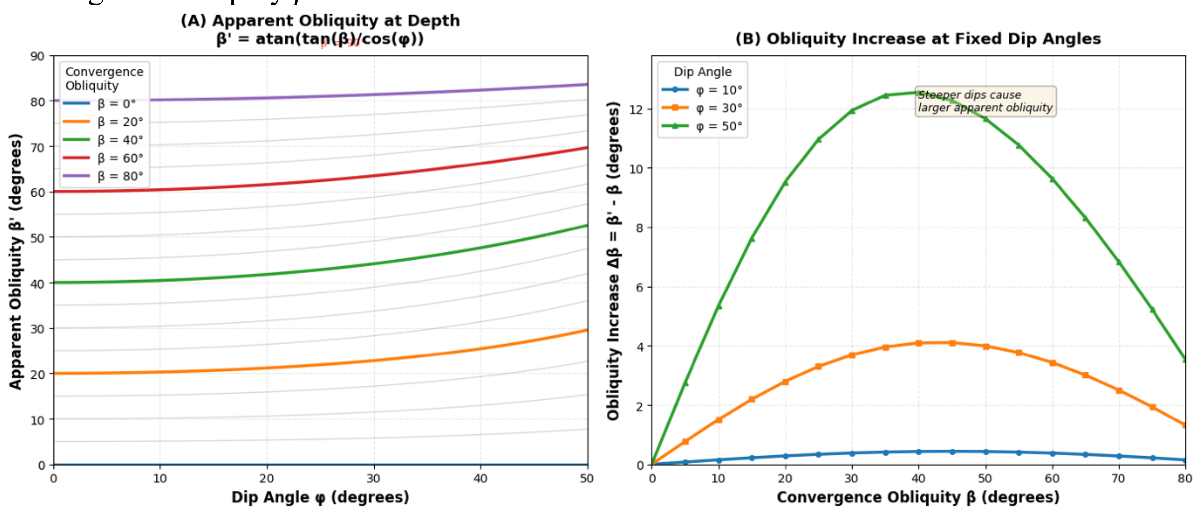

Figure S5. *Effects of convergence obliquity correction to β' as a function of local slab dip φ and uncorrected map-view convergence obliquity β.*

M2.6 Regime mapping in practice

For each filtered interface-thrust earthquake, we compute:

$$R_\alpha = \frac{\sin\varphi}{\tan(|\alpha|/2)} \quad \text{and} \quad R_\beta = \frac{\sin\varphi}{\tan(|\beta'|/2)} \quad (12)$$

using the selected fault-plane dip φ and dip-corrected convergence obliquity β'. These quantities map each earthquake onto the theoretical framework defined in the above Section M1.6 (Fig. S4).

In the implementation, specifically, events were classified using a 10% tolerance around the 1:1 line in R_α–R_β space for the 3 regimes:

1. Partitioned: $R_\alpha > 1.1R_\beta$
2. Non-partitioned: $0.9R_\beta < R_\alpha < 1.1R_\beta$
3. Anomalous: $R_\alpha \leq 0.9R_\beta$

The 10% tolerance is arbitrary but attempts to remove sensitivity near the 1:1 line in R_α–R_β space due to numerical uncertainties or small geometric perturbations.

M2.7 Determination of optimal R^*

For each subduction zone, we determine an effective population-based optimal strength ratio R^* from the distribution of partitioned events. We compare two approaches for determining R^*. First, we count the total number of partitioned events with candidate R values that satisfies:

$$R_\beta < R < R_\alpha \quad (13)$$

This criterion is consistent with the analytic model prediction that the regime boundary, defined by R, divides the convergence and slip obliquity (Fig. S4). This count-based optimal value, $R^\#$, is determined to be the candidate R^* value that maximizes the fraction of partitioned events satisfying this condition. We also separately calculated a moment-weighted optimal value, R_M, using the same criterion, but maximizing the cumulative seismic moment of events satisfying $R_\beta < R < R_\alpha$, rather than the event count. We present both results for each subduction zone in the following supplementary text Fig. S-region-C for each margin.

To characterize along-strike variabilities, we also calculated an R-interval that encompasses a target fraction of partitioned events. In the implementation, we find a narrowest possible interval $[R_{\min},\ R_{\max}]$ containing $R^\#$ that includes a target percentage (90%) of partitioned events. This interval is used to represent a range of possible strength ratio R rather than assigning a single physical strength ratio to the whole subduction zone.

M2.8 Sensitivity checks

We evaluated sensitivity to the filtering assumptions by comparing results under alternative choices of:

- centroid-based versus hypocenter-based event categorization relative to slab interface
- Slab2 uncertainty threshold for defining on-slab events;
- focal-mechanism filters, including rake and maximum selected-dip thresholds;
- uncorrected β versus dip-corrected β';
- count-based $R^\#$ versus moment-weighted R_M;

These tests show that individual subduction zones can exhibit substantial scatter, but the first-order systematics—that megathrust slip obliquity is generally lower than convergence obliquity and bounded by a dip-dependent limit—is robust.

M2.9 Independent stress- and force-ratio estimates from b-values

As an independent comparison with the population-level strength ratio R^*, we estimated relative stress levels for megathrust thrust earthquakes and upper-plate strike-slip earthquakes from their magnitude-frequency distributions. For each subduction zone, we first find megathrust thrust versus upper plate strike-slip events by two different filters: locating on slab within Slab2 depth uncertainty and having a T-axis with a plunge > 50° for thrust events (*27*), whereas locating above slab and having a B-axis with a plunge > 50° for strike-slip events (*27*). Then the Gutenberg-Richter b-values were estimated separately for both catalogs using the bin-corrected maximum-likelihood method (*33*) of Aki (1965) (*34*) (also see ref. (*35*) for recent updates):

$$b = \frac{log_{10}(e)}{\bar{M} - (M_c - \Delta M/2)} \quad (14)$$

where $\bar{M}$ is the mean magnitude of earthquakes above the completeness threshold M_c, and $\Delta M = 0.1$ is the magnitude bin width.

For the thrust catalog, the preferred magnitude of completeness M_c was chosen conservatively using a combination of the maximum-curvature estimate and a b-value stability criterion, following the logic of Nishikawa and Ide (2014)(*18*) and Woessner and Wiemer (2005)(*36*). When both estimates were available, the larger value was adopted, and a local sensitivity range of $M_c \pm 0.2$ was explored, requiring at least 200 thrust events above threshold for inclusion in the thrust-envelope summary. For the upper-plate strike-slip catalog, the preferred M_c was taken from the maximum-curvature estimate and varied over $M_c \pm 0.2$, retaining only cases with at least 10 strike-slip events above threshold. These M_c choices and their sensitivity are summarized in subsequent supplementary Fig. S-region-E. Uncertainty in b was estimated by bootstrap resampling (2000 realizations). The preferred thrust b-value was then combined with the strike-slip b-values across the strike-slip M_c envelope, and the resulting uncertainty was propagated by Monte Carlo sampling (50,000 realizations).

Differential stress σ was then estimated following the empirical relation of Scholz (2015) (*19*):

$$\Delta\sigma = \frac{A - b}{B} \qquad (15)$$

where $A = 1.23$ and $B = 0.0012\ \text{MPa}^{-1}$. For each subduction zone, thrust and strike-slip stress estimates were then combined to calculate a thrust-to–strike-slip stress ratio,

$$R_b = \frac{\Delta\sigma_t}{\Delta\sigma_s} \qquad (16)$$

We report the median R_b together with its 16–84% and 5–95% uncertainty bounds as functions of strike-slip M_c, as shown in supplementary Fig. S-region-E. In the present implementation, uncertainty associated with the Scholz calibration itself was not propagated.

To account for a more realistic geometry of the natural system in which the effective brittle-ductile transition depth of the megathrust interface may be different from that of the upper plate strike-slip faulting, from eq. (5), we additionally defined a geometry-scaled force-equivalent ratio from the b value, $R_{b,\text{force}} = R_b \times r_A$, where r_A is the ratio in effective fault area between the megathrust thrust (A_t) and upper-plate strike-slip (A_s) systems. To estimate r_A, we first estimated the seismogenic thicknesses of the two earthquake catalogs (Fig. S-region-E, bottom panel) and then scale the dipping megathrust with the mean dip angle from Slab2. Effective thicknesses for thrust and strike-slip earthquakes, H_t and H_s, were defined from depth ranges of the two catalogs, and their ratio $r_H = \frac{H_t}{H_s}$ was converted to an approximate fault-area ratio using the mean megathrust dip $\bar{\phi}$,

$$r_A = \frac{r_H}{\sin\bar{\phi}} \qquad (17)$$

The factor $1/\sin\bar{\phi}$ accounts for the larger fault area of a dipping megathrust relative to its vertical thickness, whereas the upper-plate strike-slip system is approximated as near-vertical in this first-order comparison.

The unscaled R_b is considered as an independent stress-ratio estimate to compare with the population-level $R^{\#}$ in the global cross-margin analysis. $R_{b,\text{force}}$ values are generally larger than Rb by a factor of rA from ~2 to 5.

These b-value-based quantities are interpreted as independent statistical proxies for the relative strength of megathrust and upper-plate strike-slip fault populations. They are not expected to match R^*exactly, because R^* is an effective population-level parameter inferred from slip partitioning analytic framework, whereas R_b and $R_{b,\text{force}}$ reflect stress conditions inferred from a seismology empirical relationship following Scholz 2015 (*19*) without incorporating its uncertainty for simplicity. Additionally, for margins with large along-strike variation in convergence obliquity (e.g. Sumatra or Aleutian), the overall averaged $R^{\#}$ value may be ‘contaminated’ by the low convergence obliquity region which could lead to higher value than the true stress ratio. Hence, the comparison is only used as a first-order consistency test rather than as a direct validation of the analytic model.

Fig. S6 compares the population-level $R^{\#}$ inferred from observed obliquity with the independently estimated b-value-derived ratio R_b for individual subduction zones. Horizontal bars show the $R^{\#}$ interval required to capture 90% of partitioned events, representing along-strike and temporal variability in the effective obliquity limit. Vertical bars show uncertainty in R_b from b-value estimates. Well-constrained margins generally fall near the 1:1 relation, indicating that the inferred resistance ratio under the analytic model framework is broadly consistent with independent stress estimates using b-values. This agreement is encouraging because the two quantities are derived from different aspects of the earthquake catalog: slip-direction systematics for $R^{\#}$, and magnitude-frequency distributions for R_b. The comparison also highlights important limitations. Kermadec is a clear outlier from the main 1:1 trend where its $R^{\#}$ is significantly higher than its R_b. A high $R^{\#}$ is plausible for Kermadec because it is a sediment-starved, erosive margin, where thin trench sediment and rougher interface conditions may promote stronger effective megathrust resistance (*37*, *38*). On the other hand, R_b reflects differential stress inferred from earthquake size distributions, not directly the integrated mean shear resistance used in the work-minimization model. Fluids, roughness, heterogeneous coupling and aseismic deformation etc. can therefore decouple R_b from slip-direction-derived $R^{\#}$. Low convergence obliquity may also inflate $R^{\#}$. Thus, we do not interpret R_b as a direct validation of $R^{\#}$. Instead, Fig. S6 provides an independent consistency check: where earthquake populations are sufficiently well sampled, the effective obliquity limits inferred from slip directions are broadly compatible with stress ratios inferred from b-values. This supports the interpretation that $R^{\#}$ captures a margin-wide deformation partitioning between megathrust and upper-plate fault systems.

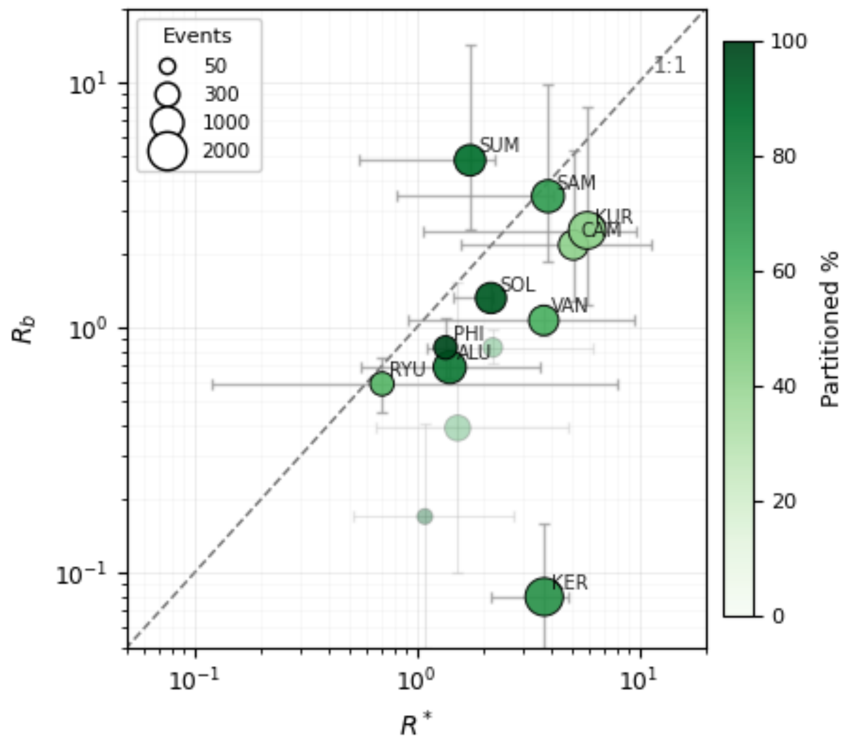

Fig. S6 Correlation between the inferred R*(R[#] here) in the framework of the analytic model (SI: M1.6 & M2.6) and the b-value-derived stress ratio Rb (SI: M2.9). Horizontal bars show the R* range capturing 90% of partitioned events, and vertical bars show the 16–84% uncertainty range of Rb. Symbol size scales with the number of megathrust earthquakes analyzed, and color indicates the percentage of partitioned events. Faded symbols indicate computed but weakly constrained Rb estimates due to low event counts or uncertain completeness magnitude (see SI: M2.9).

#	SZ	N	parti% count	parti% M0	$R^{\#}$	$R^{\#}90$ min	$R^{\#}90$ max	Rb	Rb min16	Rb max84	rA
1	**Aleutian** (alu)	1052	82	96	1.41	0.56	3.56	0.69	0.62	0.78	3.73
2	**Central America** (cam)	718	42	57	5.07	1.59	11.45	2.17	1.28	5.30	2.48
3	**Caribbean** (car)	49	92	92	1.09	0.52	2.72	0.17	0.05	0.41	3.91
4	**Izu-bonin-mariana** (izu)	400	66	72	1.53	0.65	4.84	0.39	0.1	1.54	1.19
5	**Tonga-Kermadec** (ker)	1924	72	95	3.75	2.14	4.82	0.08	0.03	0.16	7.35
6	**Kuriles-Japan** (kur)	1775	43	16	5.85	1.07	9.73	2.49	1.24	7.98	5.58
7	**Manilla** (man)	126	67	77	2.2	1.63	6.22	0.83	0.71	0.98	2.69
8	**Philippines** (phi)	262	98	99	1.35	1.11	1.48	0.83	0.62	1.09	2.06
9	**Ryuku Nankai** (ryu)	286	57	65	0.7	0.12	7.92	0.59	0.45	0.75	5.20
10	**South America** (sam)	1062	68	80	3.9	0.82	4.14	3.43	1.85	9.79	2.12
11	**Scotia** (sco)	279	72	80	2.44	0.93	4.42				0.97
12	**Solomons** (sol)	834	93	99	2.16	1.47	2.19	1.32	1.17	1.50	2.61
13	**Sumatra** (sum)	881	86	99	1.74	0.55	2.26	4.81	2.53	14.21	5.57
14	**Vanuatu** (van)	732	60	56	3.73	0.91	9.46	1.07	0.94	1.23	3.96

Table S1. Global averaged across-margin comparison. SZ: subduction name (short name) used also in supplementary text and in the code; N: total number of megathrust earthquake used for the analysis; parti% count: the percentage in count for the partitioned events over N; the percentage in total moment for the partitioned events over total moment of all events; $R^{\#}$: optimal R value that maximize number of events that are consistent with analytic prediction; $R^{\#}90$ min and max: $R^{\#}$ interval that include 90% of partitioned events; Rb: b value inferred stress ratio; Rb min and max: Rb interval range from 16 to 84 percentile; rA: cross-sectional fault area ratio between megathrust and upper-plate strike-slip (SI: Figs. S-region-E bottom panel).